Multidisciplinary research method for designing and selection of bio-inspired profiles in the conceptual designing stage

Suzana Linić, Vojkan Lučanin, Srdjan Živković, Marko Raković, Slavica Ristić, Bojana Radojković, Suzana Polić

Abstract

A multidisciplinary research method was employed with the intention to create a series of bio-inspired flattened airfoils, observe their aerodynamic characteristics, and analyse their applicability to small devices or to designs of high-speed trains, within the shortest period in the conceptual stage. A research specimen of a kingfisher, selected for biomimicry, was examined with the following methods: visual inspection, analysis of photographs, manufacturing quality control measurement with a 3D laser scanner, and microscopy. A basic multi-arc-line profile, re-engineered from the overlapped specimen shape data and based on the observations, was used for designing a series of seven derived airfoils. The aerodynamic characteristics of the bio-inspired airfoils were obtained with the panel methods at low and moderate subsonic speeds, while the small transonic difference method was used in the high-subsonic speed range. Basic and ellipse-like airfoils produce higher total drag at low and moderate velocities and higher forebody drag in the high-subsonic range when compared to derived and parabola-like airfoils. The obtained critical Mach numbers are in the range from 0.76 to 0.78, where three bionic airfoils show values equal to or smaller than the values of ellipse- and parabola-like airfoils. The profile with the shortest bio-inspired relative chord has a higher critical Mach number value than the parabola-like profile. The sonic lines above these profiles appear at close positions. The applied set of examination methods of the bio-inspired design is not time consuming and produces sufficiently good results in the conceptual stage. Therefore, a further development of unique and adjusted numerical methods and codes at pre-computational fluid dynamics run is encouraged, together with shape parameterization.

Keywords Aerodynamics · Design · Bionics · Quality measurement · Laser scanning · Numerical method

Introduction

In the last four decades, the awareness of the necessity of optimization and its implementation in a broad range of fields and activities have become a priority mainly to reduce costs and consumption of natural and energy resources as well as to improve environmental protection. However, performing these processes is justified for a well-developed physical model, mostly in the phases of a preliminary design process and the conceptual design, for which a set of favourable shapes has already been selected. The top-down path, with a focus here on the high-speed train design, leads to the main problem of a designing process that is a selection of the shapes. The aim is to create a shape that would lead to a promising direction concerning design objectives, configuration definition, and performances and processing time.

The conceptual design selection process is supported by a large number of methods based on the knowledge, functionality, geometry, reasoning, problem-solving, cases/experience, and others. The available resources show that efforts have resulted in extensive knowledge and a new way of thinking, but often at a high price, that makes decision-making even harder. The organization and hierarchy of the tasks required for the determination of the aerodynamic design of the high-speed train are illustrated in [1]. The basic task concerns the design description by using shape variables (cross section shape, area and its distribution, slenderness, etc.).

Various methods of describing high-speed train design in 2D and 3D space are reviewed in [2]. In the beginning, the 2D designs are analysed concerning mainly the high-speed train's forehead shape. Therefore, the 2D planar design is primarily intended for analysis of the effects of the longitudinal cross section parameters on the flow and, consequently, the aerodynamic drag [2, 3]. Of course, the aerodynamic performances of 3D design are subjected to the influence of the fore-body shape, dimensions, and body type (squared, rounded or sharp) [3–5]. Therefore, a 3D flow is distributed around the body (top, sides, and bottom) involving: sliding streams from the forehead to the sides; sliding stream from the sides to the afterhead; induced vortex streams over the edges and in the wake; interactions with the ground and the environment, etc. [1–5]. The pressure/velocity distribution over the contour in the longitudinal plane of symmetry is not directly scalable to the 2D case due to the flow complexity.

The most important cross section parameters of the 2D profiles are the outline shape, cross-sectional area distribution, length, bluntness, and others [2, 3]. Therefore, since a small number of parameters is needed for the description of a 2D planar profile, this approach is advantageous in the process of aerodynamic designing and it contributes to time and computational efficiency. Among many developed shape optimization methods, the Bézier curve model stands out. The Bézier curve, capable of representing enough details of the cross section, allows customization for further space-dimension addition. Furthermore, one of the design descriptions was found in the nonparametric method based on morphometry and is briefly shown on the examples of realized trains in [6]. On the other hand, the method of inverse-design is intended for adjusting the desired aerodynamic characteristics, by adjusting the velocity distribution, over the initial airfoil. In this case, the scattered 2D geometry is a result of the numerical method as shown in the Open Source code of XFOIL [7].

At the same time with the development of mathematically and statistically based methods of shape optimization, the biomimicry method made a breakthrough in science and engineering, as a sort of a shortcut, but under the one condition—the natural phenomenon and one to be solved have to be well understood. Biomimicry was initially applied to support shape optimization, but with time it has evolved towards a problem-solving approach, so that it can be said today that it has grown into a philosophy applicable in all fields of science and engineering [8]. Major efforts in applying biomimicry shape should be made in seeing the resemblance to a natural solution, understanding of the actual problem and the natural solution, selecting a specimen (in case of shape definition), decomposing a multi-physical task, and simplifying it—everything that is in the best interest of the requested functionality and physics of the problem. The Shinkansen high-speed train series from Japan is the best example how an understanding a physical and natural phenomenon has led to the solution of a multidisciplinary problem of a high-speed train entering a tunnel. The Shinkansen 500 Series train design performances, especially the rail tunnel entry, resembled the transient multiphysics event of the kingfisher's beak splashless water entry when the beak shape maintains the undisturbed water surface during plunging [9]. The bio-inspired shape of the Shinkansen train has multiple advantages such as increased operational velocity, drag and noise reduction, improved energy efficiency

and more. Unfortunately, in the biology reference sources about the kingfisher, the data required for biomimicry implementation and multiphysics research of the plunge-diving manoeuvre such as detailed morphology, surface properties, plunging velocity, path slope, hovering height are lacking; therefore, most of them have to be assumed for a certain purpose. One may note that many of flying and swimming animals (Gannets, Batoids, Sturgeons, Sawfishes, Dragonets, Sailfishes, Dolphins, Eels, Gulper-shark, duck's beak, etc.) may serve also serve as the good candidates for a bio-inspiration for the high-speed train design; but there are only few examples when they served as a biomimicry basis.

In the literature, the various methods for determining the complex shapes were reported. Novel methods of 3D laser scanning and additive manufacturing have shown advantages in biology, medicine, palaeontology, biomimicry, heritage, education, and reverse engineering. The 3D laser scanning method is a well-known high-quality method for measuring, quality inspection, and data analysis in industrial applications and many other fields. For example, an extensive study of the beak evolution was realized for the research of bird's diversity, as reported in [10]. Over the 2000 specimens from a heritage

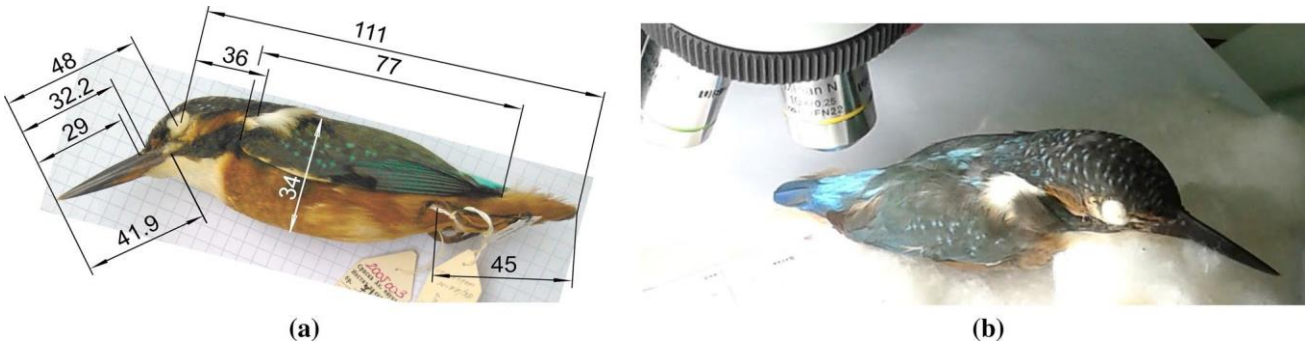

Fig. 1 Kingfisher specimen: **a** selected measures of the kingfisher; **b** microscopy setup

study skin collection were 3D scanned, including several specimens of the kingfishers, and the numerical models are published in [11]. According to the fossil study in [12], the 3D scanning is recommended as an accurate and affordable method for the determination of the complex surfaces.

To gain more knowledge about the kingfisher and to contribute to high-speed train shape design using biomimicry, we applied a multidisciplinary approach. The aim of this study is threefold. In the first place, a detailed study of the beak of a kingfisher study skin specimen, from the Serbian heritage taxidermy collection, has to reveal new details of the kingfisher natural design. The study of the beak shape and surfaces is relying on biology knowledge and methods; visual inspection; photography and microscopy; 3D laser scanning, and observing wildlife. Based on this study, a basic, i.e. natural, airfoil is created. The second task is to create different airfoils by bionics and re-engineering with operations adopted from the additive manufacturing processing (re-meshing, re-construction, modelling); and computer-aided design (CAD). The configuration of the selected airfoils is 2D planar, flattened, formed from the quarter contour curves, and symmetric in both, lateral and longitudinal directions. On the basis of the natural profile design, five derived bionic forebody nose designs are created as a power-function simplification. One design is created by the inverse-design method, from the initial bio-inspired profile. Besides the natural and bionic designs, the true ellipse and the true parabola designs were created to serve for comparison, as their shapes are highlighted in the literature for minimal drug at the transonic velocities. The third task is related to analysis and comparison of the calculated aerodynamic characteristics of different profiles in the low- and high-subsonic range. The aerodynamic characteristics of the bio-inspired shapes, under flow conditions similar to those for open rail (subsonic) and infinite tunnel running (high subsonic, transonic), were compared with a semi-ellipse and semi-parabola forms. The necessity for case simplification arises from the flow complexity, which is confirmed by the knowledge in the aerodynamics of high-speed trains and experiences from real-scale tests of high-speed trains.

Methods

Biological specimen

The kingfisher genetics is quickly adaptable to the current living conditions; thus, an amount of food significantly affects its appearance and the shape, especially that of the beak. The kingfisher mostly performs water entry manoeuvre in hunting.

After hovering, when it is searching and targeting a prey [13], a bird plunges into the water due to directional acceleration. The specific beak shape prevents the creation of recognizable waves or splashes [9, 14–16]. The kingfisher keeps an underwater direction because it does not have time and space to adjust the body pose and has the non-adapted body to control diving (palmate, strong wings with a large span and wing fineness ratio, etc.) like sea birds (gannet, pelican, etc.) [13]. Furthermore, the visual appearance of the kingfisher's body from the view of its prey serves as camouflage imitating the colour of the sky and reflections in the water. Its intensive colouration (orange, cyan, and blue) and lustre of the feathers are produced differently inside two types of feathers—by light refraction inside those filled with the nano-scale keratin sponge-like structures, and those filled with pigments (carotenoids, melanin, porphyrins, and colour anomalies) [17].

A biological specimen of the female common kingfisher (*Alcedo atthis*), from the Čukojevac, near the Kraljevo, a part of the Serbian national heritage taxidermy collection, served to this research [18]. The research study skin specimen was prepared during the year 1939 in the Natural History Museum in Belgrade (Fig. 1a) [19].

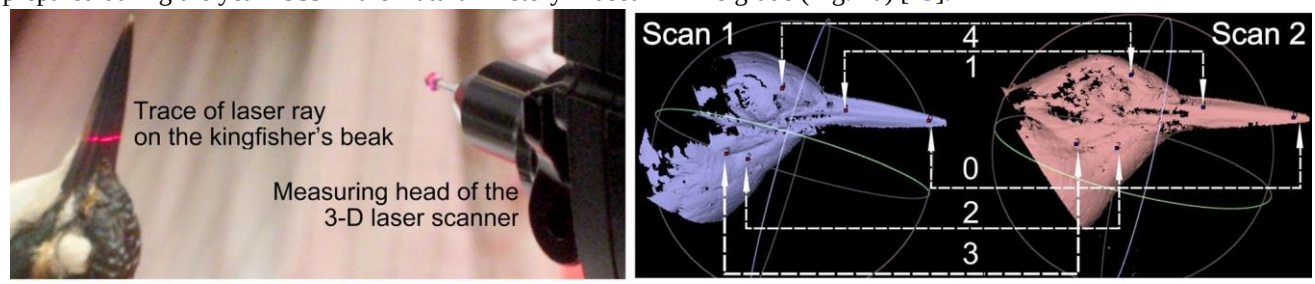

Fig. 2 **a** 3D laser scanning setup; **b** landmark points for mesh overlapping [19]

Photo-documentation and visual inspection of the kingfisher

Photographing was shown to be demanding primarily due to the optical deformations in close ranges, since it should produce good image quality and image composition, necessary for providing enough informative details. For the given reasons, about 350 photos had to be taken in different conditions, to collect first visual data about the body shape and the surface structure. The Huawei Y530-U00 and Lenovo K5 cameras were used for the photo-documenting. The object was lightened with various sources (natural, LED, and flashlight) from various positions for highlighting details. Body measuring and the body shape complexity analyses, necessary for 3D model quality control, followed visual inspection due to lack of datum. The body pose and the referent measures, selected upon modelling control requests, were taken with an accuracy of 0.1 mm (Fig. 1a) by visual inspection [20].

Microscopic observations

A digitalized microscope OLYMPUS CX 41 was used for the imaging of the accessible surfaces—kingfisher's beak sides and the upper tail covert feathers, with 40×, 100×, and 200× magnification, Fig. 1b. The additional lights (neon/ LED) from the side were used when necessary.

3D laser scanning

The 3D laser scanning method was selected as the most suitable method for measuring and describing the beak shape due to its non-destructive operation and fast data processing [21, 22]. The laser scanning setup, used in this research, contains a portable laser-scanning device, a PC with specialized data processing software, and the model—a kingfisher bird, set freely on the soft base, Fig. 2a, described in details in [19]. The Romer Absolute Arm—Portable Measuring Arm is intended for metrology, 3D digitalization, inspection of the points at a close distance, and for other purposes [21].

A series of four overlapped passes, in two lateral reference planes, relative to the beak length, were made for recording each of two clouds of points. The distance between the measuring head and the specimen was less than 200 mm. The mesh model was processed from the cloud of points and referred to the reference coordinate system of the laser scanner, with custom manufacturer's software Wilcox PC-DMIS measurement software.

The quality of laser scanning measurement depends on surface complexity and properties, equipment quality, setup configuration, environmental lighting, etc. [20, 22]. In our case, the setup was not fully adjusted mainly because the kingfisher's surfaces have the complex geometry (in macro- and micro-scales, with non-uniform surface distribution over feathers, profile roughness, waviness) and the unfavourable, non-uniform structural-optical surface properties (reflective and lustre surfaces). Therefore, the results with certain issues were expected and accepted in advance, because the focus of this work is on the beak morphology. Of course, it is recommended to overlap a series of a few dozens of scanning recordings under differently adjusted conditions, which is planned for future research.

However, each of the resulting surface meshes represents a triangular, non-conformal mesh. These two non-manifold bodies are unsuitable for a topology analysis, artistic postprocessing was thus necessary. The initial meshes were first cleaned extensively, mostly by hand and the automated tools were applied (MeshLab [23]). The initial meshes contained: the first one 1,776,433 faces with 908,874 vertices (Fig. 2b, Scan 1) and the other 2,013,102 faces with 1,026,482 vertices (Fig. 2b, Scan 2). These meshes overlapped in respect to five recognizable landmarks on the bulges, Fig. 2b points "0–4". Because of the mesh damages, only the right side of the resulting mesh was kept for generating a manifold body, applying mostly manual re-modelling (mirroring, repeated operations of cleaning, filling, fine sculpting, etc.). The resulting mesh was positioned in respect to the imported photos and the edges made by the Boolean cut with MeshLab and Blender [23, 24]. Some of the modelling issues which arose after processing of the scans, led to involving of photography and microscopy, as additional methods for magnifying specific shape and surface details.

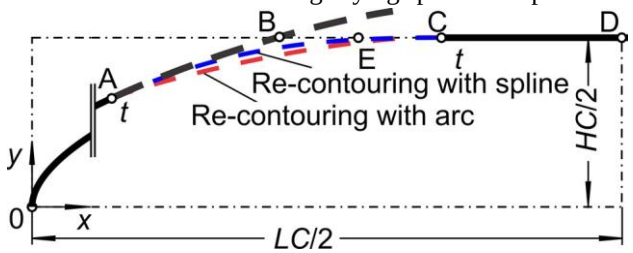

Fig. 3 Scheme of the profile re-contouring over the segments

Airfoil designing method

The profiles of interest are composed of four identical parts, symmetric to the longitudinal and the lateral axis forming the flattened airfoil, which does not follow the super-ellipse equation described in [25]. Each quarter-cross section is constructed from segments beginning from the tip. The tangent on the contour at the tip is normal to the flow direction. The natural design is created as a multi-arc-line design. Three combinations of the transition segments were applied: without transition, with arc transition and the spline transition. Each of the derived, bio-inspired, profiles was constructed to follow an algebraic function of the forebody over the segment "0–B", and to continue with a flat line, "B–D", as shown in Fig. 3. The profile smooth, spline, transition was applied. All of the transitional segments were tangentially opposed to the neighbouring segments of the nose and the central segment. Furthermore, one complex contour was created from the initial profile by the inverse-design operation. The initial quarter-cross section of the complex profile has consisted of the following segments: the power function segment of the nose, the spline transition part, a short ogive-like transition part, and the flat part at the end.

The airfoil designs were defined after several attempts that also included the preparatory calculations also, for adjusting the geometry and the setup to the software requirements. During the design operation, more airfoils with the sharp tips (ogive- and Haack body-like) were tested, but they were eventually excluded to the end because their contours could not be adjusted to meet acceptable convergence over the same set of the contour points.

Calculations

The aerodynamic problems of the high-speed trains are mostly related to the forebody design, closely dependent on operational velocity, and the train-tunnel-terrain configuration. When passing the tunnel, the train is exposed to the unsteady compressible flow that is a consequence of a flow behaviour scenario. Therefore, the criteria for airfoil selection at the high-

subsonic range are based on the c_p, cd, and M_{cr} behaviour under free flow conditions. The flow conditions in the high-subsonic range are set to be similar to those that load the train in the presence of a reflected compressible front inside the tunnel [3], during the infinitesimal time. In this situation, the inviscid flow and the wave are analysed. As the pressure/velocity distribution over the 2D profile is commented to be created under more demanding flow conditions than in the 3D case, it is assumed that the effects of 2D geometry will show similar and even strongly expressed flow behaviour. In this way, the unfavourable design details become easy noticeable.

The selected aerodynamic characteristics of the highspeed train profiles are obtained by applying the theory and codes of fluid mechanics with aerodynamics [26–32], as well as the methods and data for validation of the used codes from [33–36]. The aerodynamic parameters were calculated for the seven bionic airfoils and two airfoils with simple function contour definitions. To assure the calculation accuracy, the Javafoil software [28] was used to recalculate and reorder the contour points from the initial 2000 to 200 points, with gradual non-uniform point's density (denser at the tips). The aerodynamic characteristics of the two-dimensional airfoils were examined with XFOIL software [7], in the subsonic range of velocities, and with TSFOIL2 (with permission) [29, 30] in the high-subsonic/transonic range. XFOIL software is based on the panel method [7, 28] applicable to inviscid and viscous flow. In general, flow similarity in XFOIL is managed by selecting one free-stream turbulence level, expressed with the parameter of critical power, n, of the function e^n, and with the transition point fixation. In this work, the common $n = 9$ was used, except in one case when it was set to 12 (comparable with the flow in the lowturbulence wind tunnels) for correlation purposes. The free transition was selected. Furthermore, XFOIL treats isolated true airfoils with a cusp trailing edge to meet the Kutta condition [26]. As the main difficulty was found in shaping the trailing edge to fulfil the software requirement, the trailing edges of the actual airfoils were intentionally cut to total dimensions up to 0.006 of the normalized chord, x/LC, to succeed in convergence within 2000 iterations. On the other hand, TSFOIL2 is based on the theory of small transonic differences [29, 30], and applied to inviscid flow. It is capable of calculating surface and space flow parameters (c_p and M), predicting the aerodynamic characteristics, and predicting the shock waves in the pre-defined domain with selected mesh parameters. For the used airfoils, which present nonlifted bodies with a closed trailing edge contour, the lift coefficient was additionally set to $c_l = 0$, along with an angle of incidence, $\alpha = 0°$, employing physical scaling, and forcing the finest mesh by cutting. As previously, a total of 2000 iterations were run.

In general, the used programs are very efficient in calculations and are capable of saving a huge amount of manprocessor time in comparison with the CFD methods.

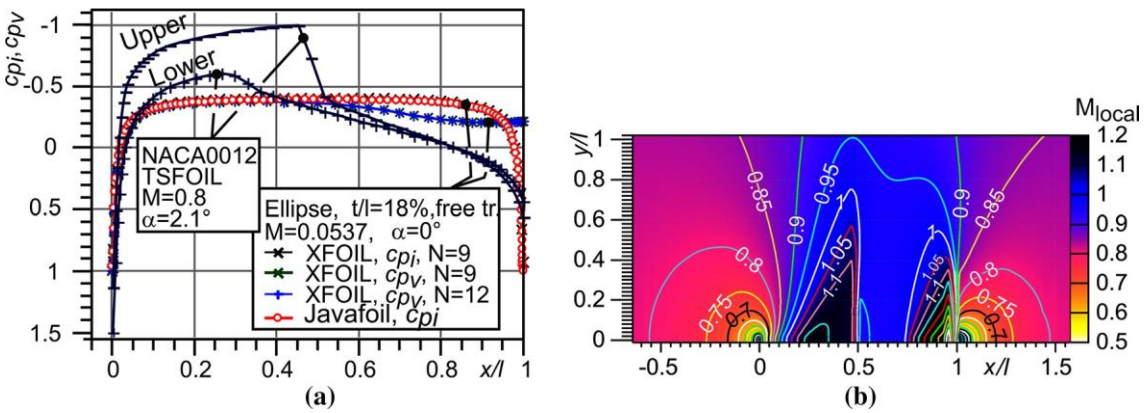

Fig. 4 Validation of the calculation methods: **a** c_p over the elliptic cylinder ($M = 0.0537$) and NACA0012 ($M = 0.8$); **b** field of M and iso-Mach contours over the ogive-like flattened half-model ($M = 0.856$)

Validation of the applied software

The calculation methods were validated for the three reference cases. The first test case is related to a wind tunnel testing of an elliptic cylinder with a relative thickness of $t/l = 18\%$ (0.1372 m × 0.0254 m) in symmetric flow, at a free-stream velocity of $V_0 = 18.3$ m/s [33]. The second case concerns the NACA0012 model tested in the T-38 tri-sonic wind tunnel of the Military Technical Institute, Belgrade, at Mach number $M = 0.8$ and an angle of incidence $\alpha = 2°$, as described in [34]. The last case presents the testing of the flattened ogive-like airfoil with the CFD method at $M = 0.856$ and $\alpha = 0°$ [36].

The comparison of the c_p over an elliptic cylinder, in Fig. 4a, shows a good agreement of the calculated values with XFOIL in inviscid flow. A slight difference in the rear zone of the turbulent layer, obtained with XFOIL, is present and acceptable due to the importance of the c_p distribution over the forebody. Equally important, the pressure distribution of the NACA0012 airfoil was estimated with TSFOIL2 software. From several quoted sets of the input data, the closest were those related to $\alpha = 2.1°$ (Fig. 4a) and $\alpha = 2°$, respectively. In particular, TSFOIL2 underestimated the c_p within a few percentages, but it predicted well the position of the shock, which is of interest for this work. Furthermore, the steady-state results of the TSFOIL2 for the ogive-like model in the transonic flow predicted well the positions of the sonic lines with shocks, Fig. 4b. The M distribution defined with the TSFOIL2 significantly differs from the reference downstream from the second pair of the shocks and beyond. This difference is interpreted as a consequence of both the applied method and the flow nature. The transient CFD study in [36] reported oscillations of the shocks and flow separation around the afterbody. However, XFOIL and TSFOIL2 are accepted for the aerodynamic calculations in the conceptual design phase to define the first decisionmaking steps.

Digital data processing

Several data processing programs were used for different workflow tasks. A series of the digital microscope records, at least five per position, with different depth sharpness, was processed with Picolay software [37] to create unique highquality images at each position. MeshLab [23] and Blender [24] software were used for mesh processing, and later has been used for cross section shape and area distribution determination. The geometric primitives of the manifold body were automatically detected by special software tools of the CAD/CAM PLM NX11 Siemens system [38]. The digitization of the upper and the lower mandible contours was done with Plotdigitizer [39], and the base profile was then re-constructed over the digitized traces with FreeCad software [40]. From the constructed contour, the coordinates of the first set of the 2D beak set as well as the ellipse contour coordinates were calculated with the Smath software [41]. Furthermore, SciDaVis was used for the contour simplifications and modifications including curve fitting, data plotting, and statistical analyses [42]. The resulting quarter-profiles were multiplied to the full profiles defined with equally spaced contour points with Excel macro. The results were visualized with Gnuplot [43] and SciDaVis software and post-processed with the InkScape [44], PaintNet [45], and GIMP [46]. To shorten the data set-up time, the various batch files (for XFOIL and Gnuplot) were prepared with Notepad + + [47].

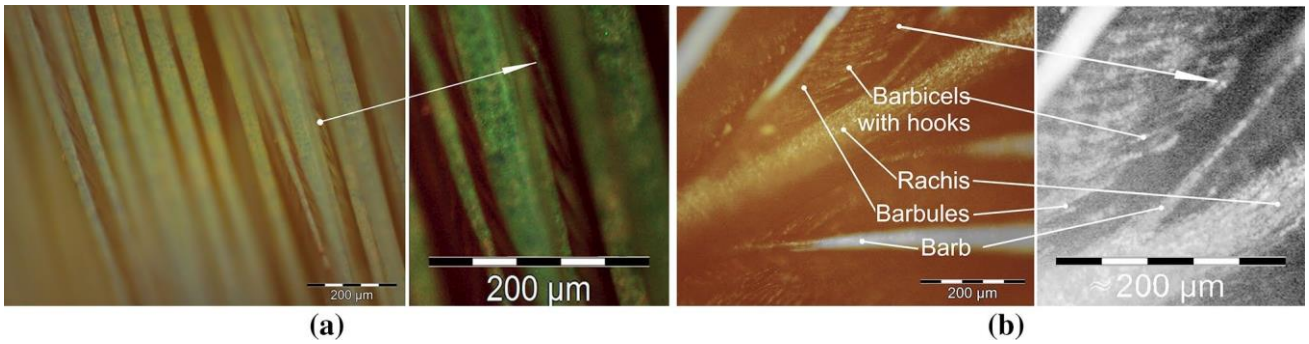

Fig. 5 Microscopic examination of the upper tail coverts vane, magnification 40×: **a** the barb's ends; **b** the middle part (additional zoomed images were edited)

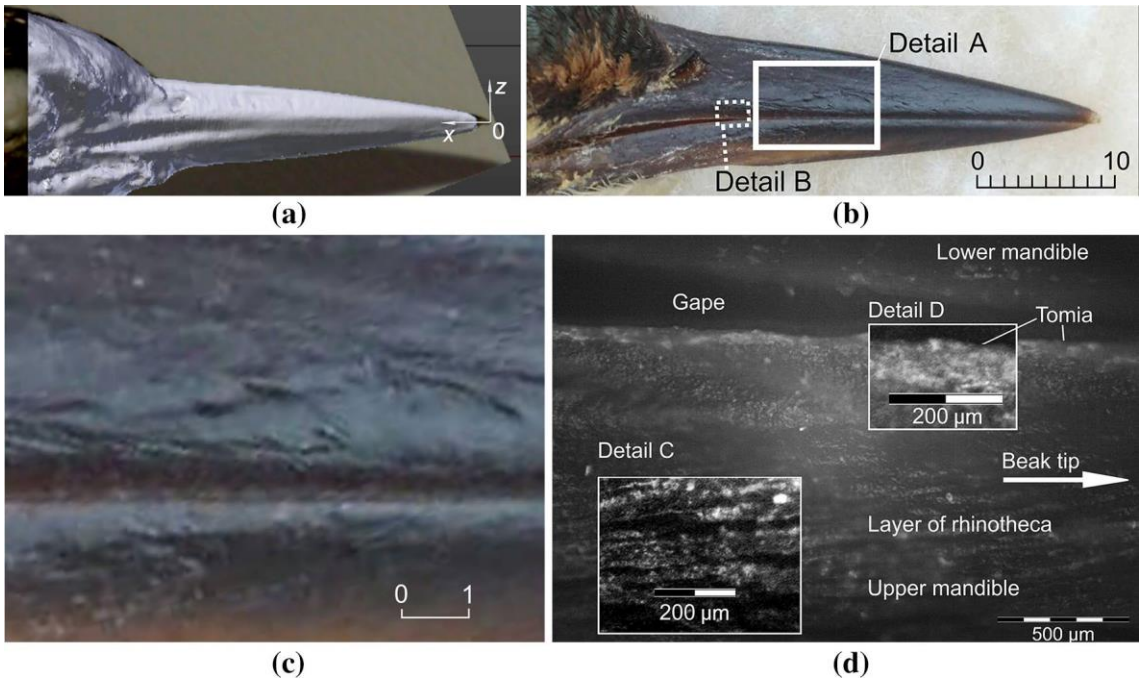

Fig. 6 Processing quality cross-control of the kingfisher's head manifold body: **a** the model contours compared with the photograph [19]; **b** the side view (credit to Maja Linić); **c** Detail A (Credit to Maja Linić): **d** detail B

Results and discussion

Description of the kingfisher's beak

A visual inspection of the beak has shown that it is advisable to collect more input data for better results of re-engineering and that the overlapping of the data from the several methods would lead to the most realistic beak shape possible. In this case, the total length of the specimen is about 155 mm, measured between the beak and the tail tips, while the maximum body width is 36 mm. The other selected measures are shown in Fig. 1a [19]. The distances from the beak tip to the forehead feathers (an exposed culmen); the anterior edge of the nostrils, and the length of the gape are the main control measures. They were intended, as reliable measures, for the cross-control of the actual scanned model and processing quality. Furthermore, the visual inspection has shown that the profile of the beak is laterally flattened, forming the triangular mandibles' cross sections with rounded corners.

The microscopy method has given a detailed view of the surfaces of the kingfisher's skin artefact with feathers, Fig. 5, and the beak, Fig. 6. A sample of blue coloured feathers of the upper tail coverts vane feathers was selected for observation (Fig. 1b). The feather structure has a complex shape in a macro-view (Fig. 5a) as well as a complex microstructure (barbules,

barbicels joint with hooks, Fig. 5b), accompanied with glossy barb's surfaces under which are seen the reflective pigmented spots can be seen. These findings are in good agreement with those reported in [17]. The feathers on the head are much shorter and fan-like shaped and less uniformly coloured. The feather structure and order partially explain the reasons for the existence of damages of the scanned model and for missing points (Fig. 2b). Feathers are recognized as the major reasons for laser ray scattering. The explanation is that scattered rays missed the paths of triangulation. Actually, the cloud of points was left without records; therefore, the facet body has to be revitalized. Consequently, the overlapping shows that the real beak tip is out of the manifold surface. The manual reconstruction of the tip did not answer to the quality requests. For that, the tip of the beak was just roundly closed to complete the manifold body, but it was excluded from the analysis of the cross sections.

The beak is represented by the images from the photodocumentation (Fig. 6a, b), 3D scanning (Fig. 6a), and images made by microscopy (Fig. 6c, d), for better understanding. Figure 6a shows the quality cross-control made by overlapping a side-view photograph and the processed manifold body. The overlapping is performed with respect to the visible edges. The coordinate system is positioned at the virtual beak tip, following the photo, at 2 mm from the manifold tip, Fig. 6a. The beak and the manifold forehead are in good agreement, except around the uncovered tip. The beak tip has probably been damaged from use, which resulted in its tiny semi-bi-convex shape.

Figure 6c, d shows the rhinotheca structure which is unevenly rough (Figs. 6b, c, Detail A). The A real rhinotheca has an ordered structure in the direction of growth. The rhinotheca roughness originates from the furrows (Fig. 6d, Detail C) which transforms to spherical forms near the tomia (Fig. 6d, Detail D).

The real gape is almost straight and partially open with a gap along the second half of the beak's length Fig. 6b. One may note the assembled manifold surfaces of the mandibles along the tomia, Fig. 6a. This sort of simplification was imported within the initial meshes, interpreted as a result of multiplied high-level reflex recordings made inside the small semi-concave space, and a gape's gap, bounded with the complex relief, Fig. 6b, d.

The curviness of the effective beak profiles is present in all directions as well as waviness. Furthermore, the plane containing the specimen's culmen and the gonys is softly skewed and curved about the ideal plane of symmetry by nature, almost immeasurable. The common lens observations show the presence of the relief all over the rhinotheca and the gnathotheca.

The numerical maxilla has shown the surface waviness in the form of repeated bump-like strips along the length with depths in the range of the measuring accuracy (most about 14–17 μm, and one of 83 μm, measured within the manifold), Fig. 6a. On the contrary, a real surface is mostly wavy alongside the beak depth in micro- and macro-scales with enhanced rounded edges of the culmen. It has been interpreted that the numerical surface waviness is recorded during movements of the measuring head, while the real imperfections are created during rhamphotheca growing and hunting manoeuvre.

The post-processing of the manifold was a time-consuming operation, done in three passes, and it took several weeks. For the better results and for saving time, it is recommended to create a few dozens of initial scanned models and to investigate applying different coatings (thin and matte) to beak artefacts that would improve the scanning quality.

The quality of the resulting manifold body was assessed as good in correlation with the presented results for the same specimen presented in [11]. Both, the manifold body of the current specimen and the mesh model from [11] show the artificial waviness of the mandible surfaces, and the contours of the culmen and the gonys are both irregular. The lateral surface waves over all surfaces are interpreted as a consequence mainly of the measuring method as well as of the surface complex topology and its optical properties. The current model has a cut beak tip, compared to the real specimen and the model [11]. For that reason, the bionic contouring relied more on the photo-images, while the manifold body was employed for the shape study. Besides, the gaps of both numerical models are closed in accordance with the recorded cloud of points.

The shape study has been employed Computer-Aided Engineering tools [38] for detecting the geometric primitives automatically. The geometric primitives were detected in two opposed curvature sensitivity rates, 10/100 (Fig. 7a) and 90/100 (Fig. 7b). Both curvature sensitivity rates give similar results about the tip. This observation shows a distribution of a large number of primitives and a huge set of their properties (dimensions, orientations, etc.). Therefore, the facet body is too complex for direct implementation into, for instance, to additive manufacturing of the experimental model, but it is suitable for use as a background model for the bionic application, and for that, the actual model preparation is sufficiently good.

The review [3] reported that the effective shape, intended to reduce the impulse wave, is one that looks similar to a half-wedge, the shape of which is described with the almost linear longitudinal normalized cross-sectional area distribution of the forebody further from the nose tip. From the fourteen cross sections of the artificial model of the kingfisher's beak, Fig. 8a, the normalized longitudinal cross-sectional area distribution is obtained, Fig. 8b, which was firstly commented in [19]. The cross-sectional area distribution of the kingfisher's beak facet, compared to the recommendations from [3], has shown the lower values than the optimal ones. The cross-sectional areas would be even smaller if the mesh closings along the gap were more precise. Accordingly, it was interpreted that the kingfisher beak design as a whole is not adequate for bionic application but its parts certainly are. Hence, the design partitioning was selected as an adaption measure, i.e. as applicable to the conventional highspeed trains. The culmen was selected as a basis for design development due to its elongation, *i.e.* fineness ratio, $\varepsilon \approx 8$, read from Fig. 8a (for the gonys it is about seven, for the symmetric top-view contour it is about eleven).

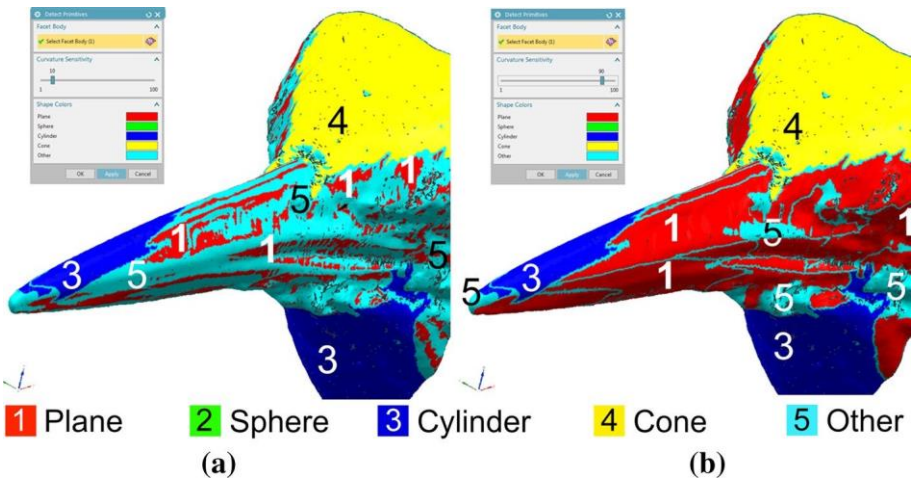

Fig. 7 Curvature sensitivity analyses of the facet body from [38] with the rates of **a** 10/100; **b** 90/100

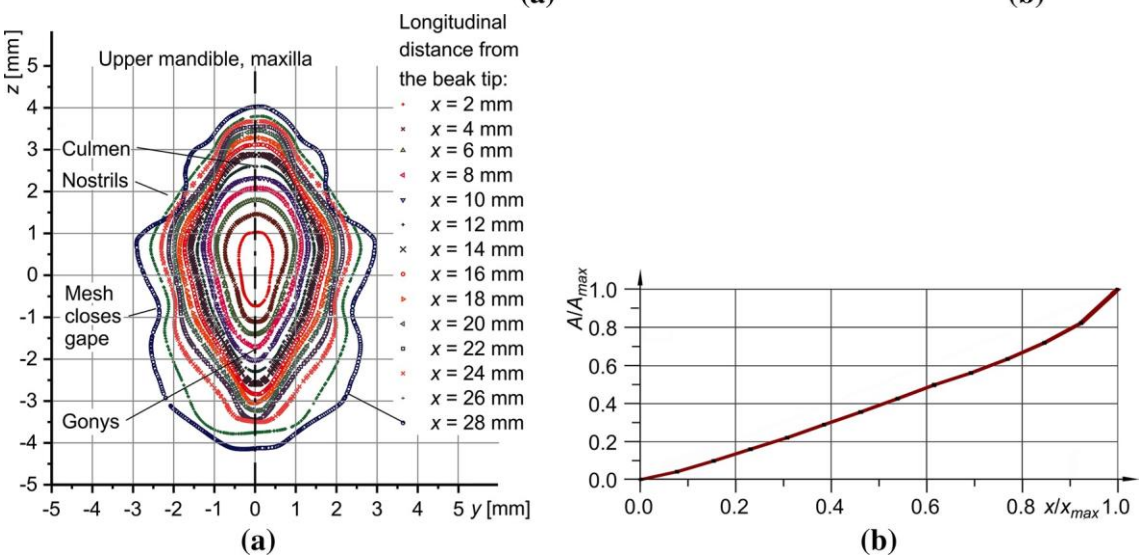

Fig. 8 Selected geometry properties for the bionic application, firstly reported in [19]: **a** A set of vertical cross sections positioned in accordance with the virtual beak tip position; **b** the cross-sectional areas distributed along the beak length

Nature-based profile design

The nature-based profile design has been adopted to follow as much as realistically the biological form of the longitudinal cross section of the kingfisher's beak culmen as realistically as possible.

The previous studies have shown that the flow around a 2D profile can make a good prediction of the behaviour of pressure/velocity distribution over the contour at the longitudinal plane of symmetry of a 3D flattened body. Thus, a 2D profile contributes to an easier recognition of the unfavourable design features that will be transferred to a 3D case later. Therefore, a 2D planar profile configuration was selected. Furthermore, the planar 2D type was selected for the analysis of the design effects on the pressure coefficient, c_p, distribution, and drag coefficient changes among different designs at various velocities. The ground effects were eliminated by attaching the two 2D planar profiles along the bottoms. In addition, the planar type of profiles is valuable for a future possible applications of water entry tests in hydrodynamic studies, inspired by the studies in the field of shipbuilding [19, 48]

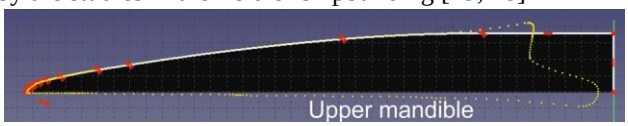

Fig. 9 The construction of the natural quarter-airfoil profiles D2/ D2RAD over the digitized beak contour (yellow dashed line)

The bio-inspired point of departure was a digitized maxilla contour (design D1), the dashed line in Fig. 9. The initial quarter-airfoil contour was constructed, over the D1 "noisy" contour, with arcs and lines, without the contour transition (design D2). The re-contoured airfoil, D2RAD, was constructed from the eight arcs (each defined with the radius, *R*, the displacement of the radius centre along the *x*-axis, *m*, the displacement along the *y*-axis, *n*, and the initial coordinates, x_b and y_b), two lines (defined with the coefficient, *k*), and the flat central-body as Table 1 and Fig. 9a describes. The half-chord length is LC/2 = 37.50 mm, half-height *HC*/2 = 3.519 mm, and $\varepsilon_{forebody} \approx 6$.

Table 1 Description of the D2RAD's quarter-chord, with 11 local segments

No.	Pt	*k* (mm)	*R* (mm)	*m* (mm)	*n* (mm)	x_b (mm)	y_b (mm)
1			0.114	0.114	0.003	0.002	0.025
2			1.040	0.863	− 0.541	0.022	0.070
3		0.711				0.260	0.306
4			1.385	1.212	− 0.717	0.410	0.412
5			5.431	2.492	− 4.555	0.774	0.597
6			50.510	13.000	− 48.392	1.225	0.726
7			38.867	10.367	− 37.051	1.576	0.809
8		0.164				4.074	1.303
9			181.114	34.628	− 177.219	5.304	1.505
10	"A"		67.736	25.403	− 64.217	19.734	3.281
11	"C"					25.403	3.519

The derived bio-inspired profile designs

The bionic contour was derived from the natural contour of the D2 after several approximations due to the existence of hardly noticeable semi-bi-convexity about the nose tip. The semi-bi-convex contour is expected to produce the local unfavourable and sudden drops of *cp*. The finally selected power-function followed the nonlinear fitting function (scaled Levenberg–Marquardt algorithm with a tolerance of 1e-06), in the length of $0 < x \leq 23.879823$ mm ("0–B"), as given in Eq. 1:

$$f(x) = (ab/c)(1+ x^c b/c)^p \quad (1)$$

where the fitting function coefficients are $a = 1.216470e{-}06$, $b = 3.518924$, $c = 23.879832$, $d = 2.175435$, $e = 0.036164$, and a the power of the function $p = 172.936470$, obtained through 644 iterations with the coefficient of determination R2 = 0.99909.

The scheme of design constructions is given in Table 2, following Fig. 3. The natural contour is reconstructed from the examinations of the kingfisher's beak, while the bionic contours were following Eq. 1, both ending in the "B" point. The true ellipse and the true parabola profiles were calculated in the "0"–"B" length, and afterwards they were smoothed in the "A–B" length.

Figure 10a illustrates the derived contours of the bionic quarter-profiles. Figure 10b shows the initial relative velocity distribution over the half-chord (the ratio of current and free stream velocities), q/V_{inf}, and re-designed with XFOIL's Mixed-Inverse Design Routine, QDES, with the interactive command for modifying, MODI, [7]. The re-designed q/V_{inf} distribution determined the quarter-profile MIXMOD contour. This airfoil covers 3% of the half-chord with the bionic contour from the tips. Moreover, Fig. 10c shows the gradient of the contours, d(y/LC)/d(x/LC), with a foreground detail of the transition zone, at which the first appearance of the sonic lines is expected.

Aerodynamic characteristics of the bio-inspired airfoils

With an awareness that there is no unique design capable of meeting all the operational requests, the authors have selected the high-speed train design priorities as follows: (a) smooth pressure distribution over the nose and the contour transition zones; (b) lower airfoil drag coefficient in the low- and moderate-subsonic range; (c) lower nose (upstream) and wave drag coefficients in the high-subsonic range; and (d) placement of the sonic line further from the nose tip.

The airfoil aerodynamic characteristics in the range of $M \leq 0.5$, were obtained with XFOIL and those in the range of $0.5 \leq M \leq 0.8$, with TSFOIL2 (for inviscid flow). Table 3 lists the low and moderate subsonic Mach and Reynolds numbers, Re, used in this work.

Table 2. Scheme of profile's designs constructions

No	Profile part	Forebody	Contour transition			Flat body
	Segment	"0–A"	"A–B"		"B–C"	"C–D"
	Design					
1	D2RAD (Table 1.)	Natural contour, Eq. 1 segments 1–10	Arc, segment 10–11			Flat from segment 11
2	D2F	Natural contour, Eq. 1	Spline			Flat
3	D2	Natural contour, Eq. 1		Flat		
4	D3N	Bionic contour		Flat		
5	D4F	Bionic contour, Eq. 1	Spline			Flat
6	D6	8% LC of D4F	Spline			Flat
7	MIXMOD (Fig. 10b)	Initial: D4F	Initial: spline "A–E" Ogive "E–C"			Initial: flat
8	DELLIF	True ellipse	Spline			Flat
9	DPOWMOD	True parabola	Spline			Flat

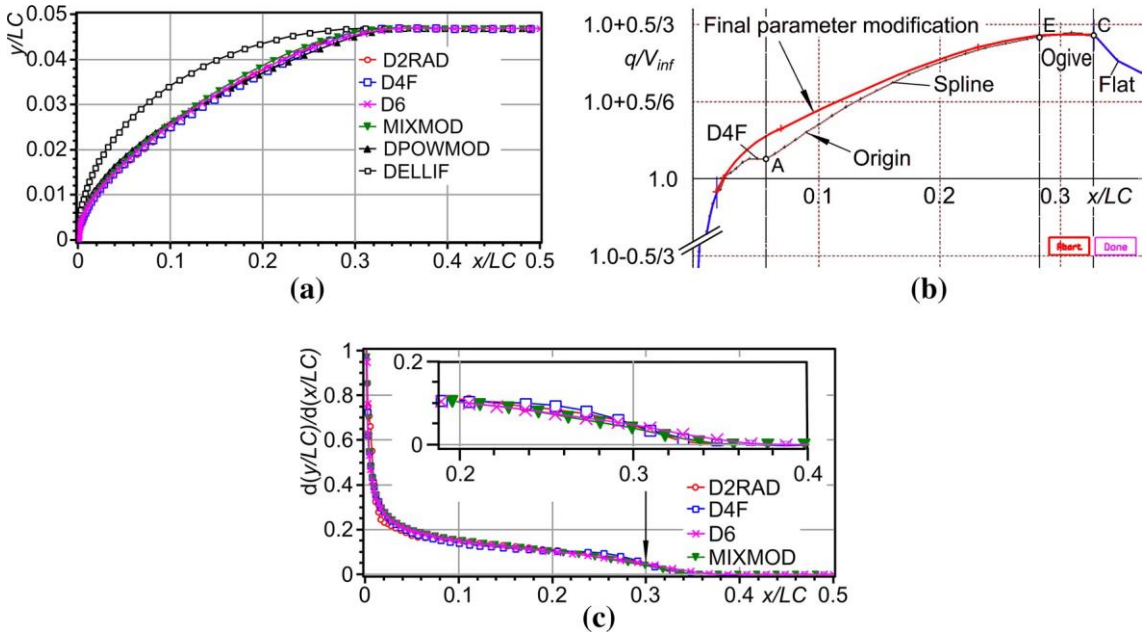

Fig. 10 Definition of designs: **a** derived bionic quarter-airfoils **b** initial (black line) and modified q/V_{inf} by the inverse-design operation (red line) of the MIXMOD airfoil at $M = 0.3$; **c** the contour gradients of four bionic airfoils along the half-chord

The c_{pi} distributions around the natural-based profiles in the inviscid flow have served for the selection of a recontouring shape at the transition zone along the normalized length $0.2 \le x/LC \le 0.4$ at $M = 0.3$, Fig. 11a. The comparison of the *cpi* distributions for different designs, natural and bionic, for $x/LC \le 0.4$ at $M = 0.3$, is shown in Fig. 11b. The effects of three different transitions on the *cpi* distribution have shown that smoothing is necessary where the spline function was selected as is favourable, Fig. 11a. The natural design, D2RAD, with the arc contour transition has shown an extreme value ($x/LC \approx 0.01$) as well as the "wavy" behaviour of c_{pi} in the zone ($0.01 \le x/LC \le 0.07$). The improper c_{pi}

Table 3 and moderate subsonic Mach List of the used low HC1 (m) HC2 (m) and Reynolds numbers for beak scaled model and train scale airfoils

HC1 (m)		HC2 (m)	
0.007		7	
M	Re	M	Re
0.0029	480	0.1	1.63e+07
0.0059	960	0.2	3.26e+07
0.01	1600	0.3	5e+07
0.0147	2400	0.4	6.61e+07
0.0294	4800	0.5	8.15e+07

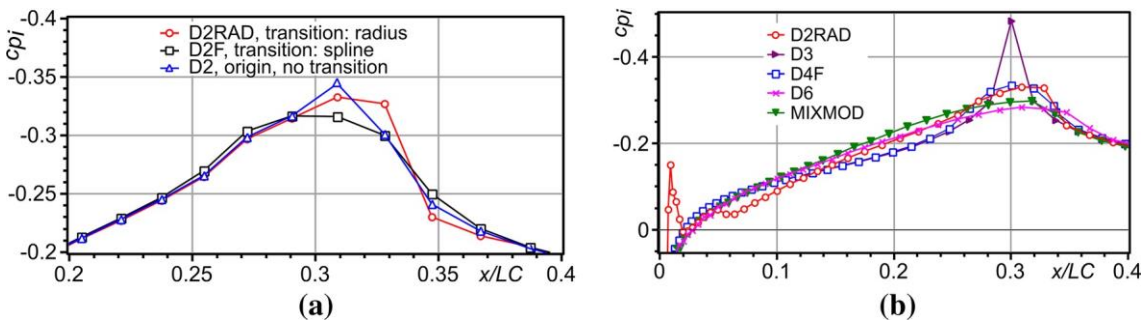

Fig. 11 The c_{pi} distribution, $M = 0.3$, Re = 5e+07 **a** for three nature-based profiles with different contour transitions, $0.2 \le x/LC \le 0.4$, **b** for the five bio-inspired profiles, $x/LC \le 0.4$

distribution over the nose is commented as a result of the contour gradient changes due to the profile geometry, that generates bubble separation. A similar effect was expected due to a generally accepted opinion that the kingfisher's beak is naturally designed for efficient water entry, but the similar cases or descriptions were not found in the available literature. The power-function profile, D3, showed an extreme value due to the non-smoothed transition; on the other hand, it generated a smooth *cpi* distribution in the nose zone. Therefore, the bionic fitted function fulfilled the task. The additional contour transition for the D4F design done with the spline has given a complete re-design solution with a smooth c_{pi} distribution all over the half-chord. A more uniform smoothness of the *cpi* distribution is generated by the D6 and MIXMOD designs. Although the smoothest *cpi* distribution is generated over the D6 and MIXMOD forebodies, a complex and bifurcated flow over the afterbodies is expected according to study [36]. Above all, special attention should be paid in case of applying a smooth transition contour to the 3D cases in viscous flow, because of the superposition of the top and side streams over the afterbody and further in the wake.

The c_{pi} surface distributions, in a range of $M \leq 0.8$, along the normalized chord, related to the airfoils in the following order: (a) D2RAD, (b) D3, (c) D4F, (d) D6, (e) MIXMOD, (f) DELLIF, and (g) DPOWMOD, are shown in Fig. 12a–g. Each shape of the *cpi* surfaces is emphasized by a hundred contour "bspline" lines. The slight differences in the c_{pi} values about M = 0.5, Re = 8.15e+07, are interpreted as a consequence of the implemented numerical methods and different treatments of compressibility. XFOIL includes the additional compressibility correction after Karman-Tsien [7]. One may note that because of the method for compressibility treatment of the XFOIL use M is limited to ≤ 0.5 even though it is justified for use in broader ranges. Thus, the c_{pi} surface deformations over the lengths of the contour transitions are most significant. This behaviour is noticed in all the profiles (except in those elliptic-like), with transformations from weak discontinuities to the strong jumps with a velocity increase, characteristic for cases of shocks. Therefore, depending on shock intensity, the designs are ranked from the weakest, DELLIF, with an almost unrecognizable shock, through D6, MIXMOD, DPOWMOD, D2RAD, and D4F, to, finally, D3. The D2RAD design shows the c_{pi} surface discontinuities over the nose in the whole range of M (similar as in Fig. 11), while the c_{pi} distribution over the transitioned contour is similar to those for
D4F and DPOWMOD. The D4F and DPOWMOD profiles indicate a completely similar and continual c_{pi} distribution change due to similar power-functioned designs, where D4F demonstrated a more gradual c_{pi} change over the nose but a slightly stronger change over the transition. The similar D6 and MIXMOD designs present an even more gradual c_{pi} change in the nose zone due to the smallest contribution of the bionic shape, about 8% and 3% of the half-chord, respectively, and create less strong shocks over the length of the contour transition. The c_{pi} distribution in D3 design illustrates an unfavourable effect of the non-smoothed contour on shock appearance.

In simplified conditions, in the cases when the train runs inside the tunnel and the air flow blows to its nose, the train is assumed to be loaded with the transonic flow under certain circumstances, as in the real situations reported in [3, 9, 49, 50]. The complex flow around the train, especially when the train passes the tunnel, is transient in reality. However, in order to simultaneously satisfy the calculation and the flow conditions for transient flow simplification, the moments at which the specific flow conditions occur were separated and treated as steady due to their infinitesimal duration. As it is well-known, the aerodynamic calculations in the transonic range are faced with many problems, from determining flow oscillations, wake, shock excitations, etc., to convergence. On the other hand, we have learned from practice given in [49, 50] that two different train designs may cause very different time distributions of pressure gradients and, as a consequence, display different behaviours of the impulse waves, although the total change of pressure is not dependent on the forebody design but on the running velocity and

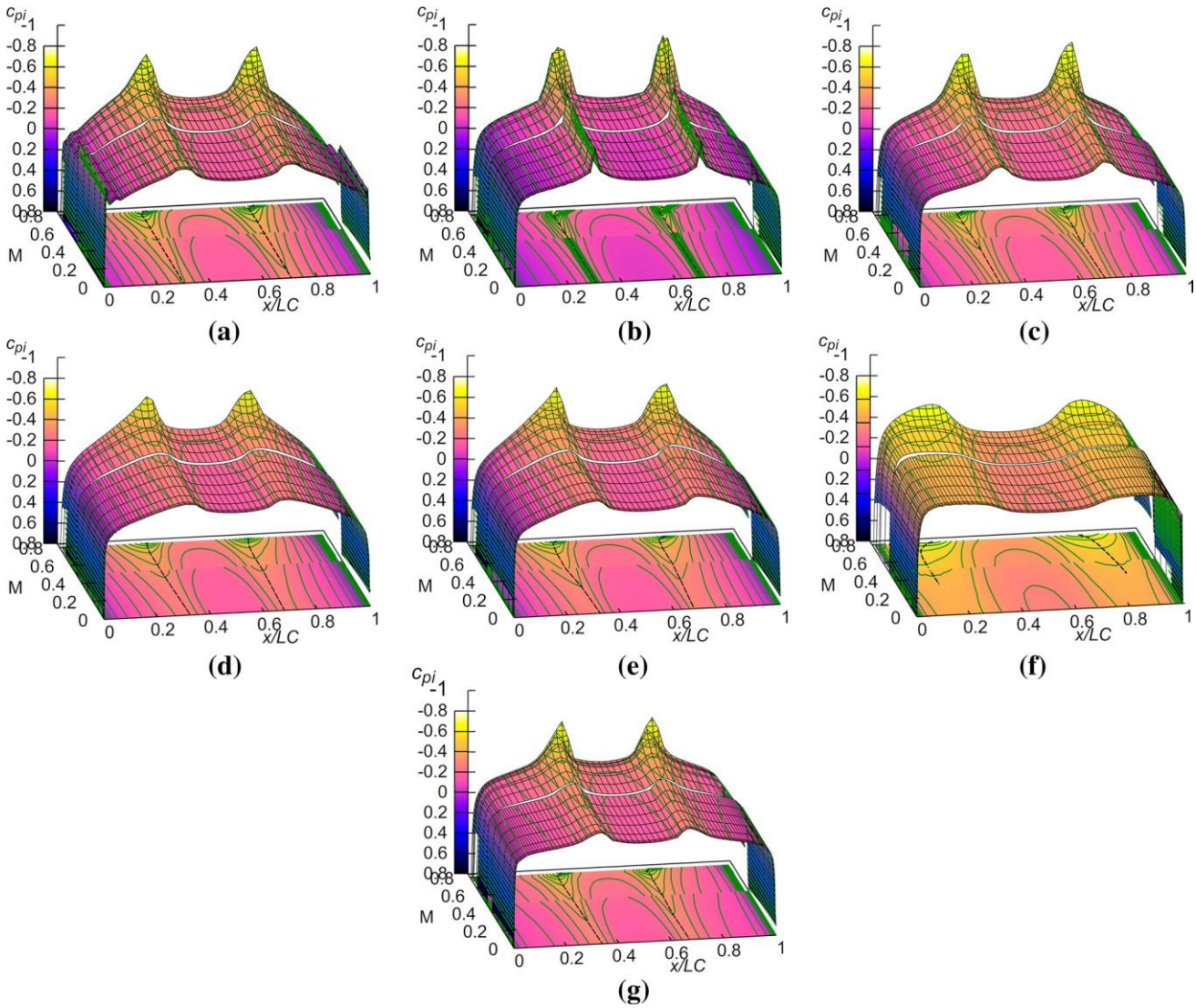

Fig. 12 The c_{pi} distribution over the upper sides of the airfoils' in the range $M \leq 0.8$ **a** D2RAD, **b** D3, **c** D4F, **d** D6, **e** MIXMOD, **f** DELLIF, and **g** DPOWMOD (Re according to Table 3)

the blockage ratio. For this reason, the c_{pi} distributions along the equidistant line to the chord (the one nearest to the imaginary tunnel wall defined with TSFOIL2 mesh is at y/LC = 0.11, HC2 = 7 m) were tested in a family of airfoils at M = 0.5. Here, a very similar influence of the forebody shape on the surrounding was noted, except for the ellipselike shape, which was expected to produce a stronger influence, Fig. 13a. The vicinity of the negative extremums of the saddle-like c_{pi} distribution confirms that the selected length of the central body is short for pressure recovery. However, as the main interest is in the selection of the forebody shape obtained with selected software, the choices were adopted as adequate and will be employed in future investigations. Afterwards, further search for the reliable guides, *i.e.* criteria, in the airfoil forebody design process led to the analysis of the c_{pi} sensitivity to contour variations. The c_{pi} sensitivity is represented by the dependence of the derivative of *cpi* in respect to the derivative of the contour function $DCP = \mathrm{d}c_{pi}/[\mathrm{d}(y/\mathrm{LC})/\mathrm{d}(x/\mathrm{LC})]$ to the derivative of the contour function $\mathrm{d}(y/\mathrm{LC})/\mathrm{d}(x/\mathrm{LC})$, as in the example shown in Fig. 13b. The calculations were done for L_{ref} = HC2 = 7 m in low turbulence flow with n_{cr} = 12 at M = 0.3, in accordance with Fig. 12. Figure 13b makes the effect of the difference in shapes and their influences on c_{pi} clearer by introducing the *DCP* especially over the nose shape. Now, the *DCP* curves related to the group of bionic and ellipse-like contours (except of the D2RAD profile) are equidistant, almost

linear, in the nose zone. The *DCP* related to the parabolalike contour bridges the *DCPs* of the bionic and ellipse-like contours, having similar values and behaviour to those of the

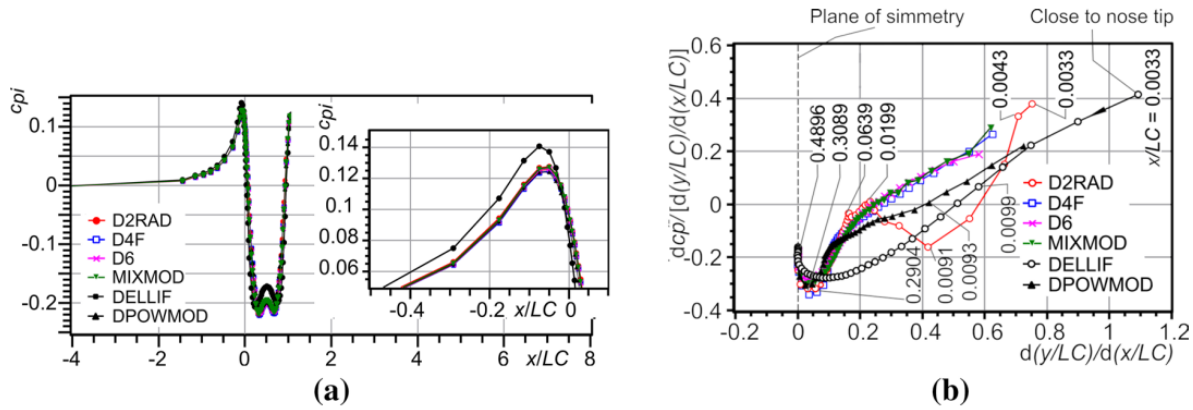

Fig. 13 Sensitivity of the c_{pi} behaviour: **a** on airfoil shape followed along the equidistant line to the chord at M = 0.5, Re = 8.15 e+07 **b** by DCP to the changes of contour gradient at M = 0.3, Re = 5 e+07

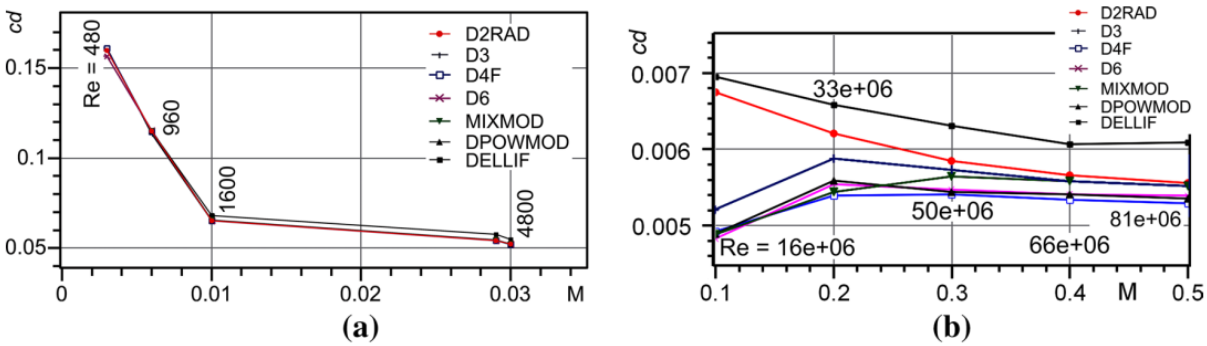

Fig. 14 Values of cd **a** for small models at very low M, L_{ref} = HC1 = 0.007 m, **b** for large models at low and moderate subsonic M, L_{ref} = HC2 = 7 m, n_{cr} = 12

ellipse-like shape near the nose tip, and similar behaviour to the bionic ones in the zone of contour transition. However, the *DCP* function of the D2RAD design crosses over all the others, over the length between the nose tip and the transition zone due to the shape segmented in nature. The contour transition geometry depends on the nose tip geometry, the beginning of the transition zone, and its length. Therefore, *DCP* sensitivity on to contour transition is interpreted as a reliable criterion for design selection, where the dependences from curved- to bell-shaped are convenient, while the bell-shaped ones are desired. The *DCP* sensitivity analysis is regarded as a reliable and simple method for design quality control. Nevertheless, as it may be seen from Fig. 13, a sufficiently wide parameter space is available for creating a whole palette of airfoils not necessary bionic, from the ellipse-like to the wedge-like shapes, when parameterization becomes a future concern. Of course, the extensive transient CFD investigations are recommended in the next step, for broader Design of Experiment, and for more precise conclusions.

Figure 14a shows the drag coefficients, cd, for seven small scale airfoils (LC1 = 0.075 m, L_{ref} = *HC1* = 0.007 m), in the interval of 0.5 m/s ≤ V ≤ 10 m/s, at free stream velocities similar to those of the kingfisher's in plunging. At very low velocities, the ellipse-like profile has the largest cd, as commented, due to the longest wetted contour producing the largest drag component related to the skin friction, where the difference of the current values from the mean values of the other profiles is gradually increasing. The long mod of cd than the previous ones, Fig. 14b. This case is set to simulate a train running on open track. The highest cd was calculated for the ellipse-like profile, again, followed by the multi-arc-line profile, D2RAD. Their cd values are higher even than of the D3 with sharp contour transition. The MIXMOD configuration shows unfavourable cd values at velocities of interest for high-speed trains, above M = 0.3, which are partly equal to the cd of the

D3 design. The parabola-like profile and the least-bionic- profile (DPOWMOD and D6, respectively) create similar cd dependences over the M interval. The lowest drag is produced by the power-fitted profile, D4F, and close to the cd values of the previous two designs at $M \geq 0.3$, which makes all the three designs (D4F, D6 and DPOWMOD) applicable in this M range.

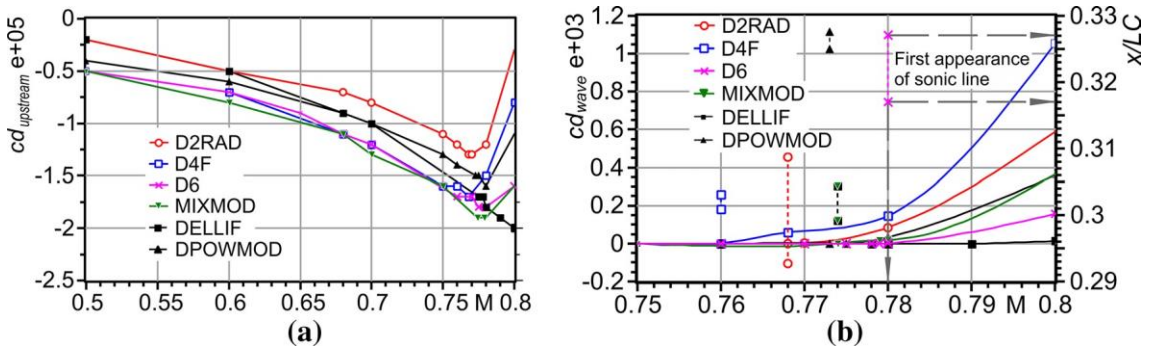

Fig. 15 The drag coefficient components against M for different profiles **a** The inviscid $cd_{upstream}$, **b** cd_{wave} and the zones of the first appearance of the sonic lines

In the range of moderate and high-subsonic velocities, $0.5 \leq M \leq 0.8$, the coefficient of upstream profile drag, $cd_{upstream}$, has been adopted as the measure of the forebody drag coefficient, Fig. 15a while cd_{wave} has been seen as a tool for analysing of Mcr and tracking of the first appearance of the sonic line, Fig. 15b. Additionally, c $d_{upstream}$ has become a comparable parameter due to a neglectable total profile drag value resulted from the streamwise force annulling, expressed within d'Alembert's Paradox [26]. The increase in velocity to high-subsonic again produces the largest cd $_{upstream}$ for D2RAD. The DPOWMOD and DELLIF have the similar and second in order $cd_{upstream}$ values, while for the group of bionic profiles (D4F, D6, and MIXMOD) has the lowest $cd_{upstream}$ values (especially the MIXMOD), as opposed to its cd order at low-velocities. Their $cd_{upstream}$ values are even lower than those of the parabola-like profile. Therefore, it has been assumed that the bionic profiles are suitable for high-speed train design at $M \leq 0.8$ in accordance with the calculated values of cd.

Consequently, it can be concluded that several parameters play a significant role in reaching M_{cr} and the production of cd_{wave}, such as: the precision of the contour definition described by the number and distribution of the contour elements (the maximum possible number of elements was used); stepping rate of M; contour gradient distribution along the chord; and *DCP*, among others. However, the contour definition quality is limited within the software code and the maximum number of contour points is used with a gradual increase in point density from the central-body to the nose tip. It is commented that M_{cr} and the positions where the sonic line firstly appears over the half-forebody are in agreement with the contour gradient behaviour.

Furthermore, the calculated wave drag, cd_{wave}, increases in the case of all airfoils (except for the ellipse-like one) obtained with a step of $\Delta M = 0.001$ in the symmetric case at $\alpha = 0°$ and at velocities larger than critical, so that its significance as a total drag fraction becomes more important than the significance of the profile shape, Fig. 15b. Because of the complex nature of the flow behaviour around the elliptic cylinder in the transonic flow, this model is excluded from the analyses in this part of the work. The c d_{wave} values and their gradients increase oppositely to the M $_{cr}$ values. The profile with the most intense change of the contour gradient in the contour transition zone (D4F, Fig. 10b) experiences the lowest $M_{cr\,D4F} = 0.76$, sonic lines appear at x/LC = 0.3, and it creates the largest c d_{wave}. On the contrary, the favourable profile with the smoothest contour transition gradient change (D6, Fig. 10b) reaches M $_{cr\,D6} = 0.78$, and the sonic lines begin further down the contour, at x/LC = 0.317, and create the lowest cd_{wave} and its gradients. The relation between the data shown in Figs. 10 and 13 has displayed higher critical Mach numbers over the forehead might be controlled by the smoothness of the transition contour between the nose and the central body. A smoother contour shows higher values of the critical Mach number of the forehead. On the other hand, in the case of the symmetric model, the complex flow over the afterbody can trigger bifurcations and separations. The unstable flow over the afterbody influences the wake thus tending to null the favourable aerodynamic effects of the forebody design. The research [36] and others on this topic, reported the complex phenomenon of bifurcation in transonic flow, "self-exciting oscillations of shock waves" obtained by CFD [36], boundary layer separation in the transonic flow around the ogive-like flattened airfoil, as well as the presence of the multiple solutions, in a certain velocity

range, depending on the initial conditions. From there, it is recommended to continue work employing transient CFD studies as well as wind tunnel investigations for more precise results.

From the previous outputs, it was concluded that the calculated pressure distributions around the foreheads of natural, bionic and simple-function profiles (Figs. 11 and 12) are following the flow behaviour described in [4, 51–53]. Some comments on profiles' aerodynamic characteristics are first referred to the low- and moderate subsonic velocities. The comparison of the pressure distributions over different bionic and simple-function profiles with the high-speed train's contour at the central plane from [51] shows a good agreement of the results. The cp in [51] around the nose tip shows a decreasing trend somewhere in between the decreasing trends obtained for bionic (D4F profile) and ellipse-like (DELLIF profile) in accordance with the relations of the relative radiuses. In the transitional region, the correspondence is found between the obtained sudden pressure drop for an unsmoothed bionic profile, D2 and D3 (Figs. 11, 12) and [51] due to a sudden change of the contour gradient. The influences of the high-speed train design (cross-sectional area distribution and length) on the environment are compared for the six profiles (Fig. 13a) and similar ones reported in [52]. The pressure changes created along the equidistant measuring lines in these cases are shown to be in good agreement in behaviour over the regions of the forehead and the afterhead. However, the pressure recovery over natural, bionic and simple-function profiles, in the region of the central body, is not realized, so it differs significantly from [52] due to the selected short length of the central body without any coaches between the forehead and the afterhead. In the next step, the correlation is established for the M = 0.8, for the case of a high-speed train in virtually passing through a tunnel. The correlation is established with the results obtained for the projectile-like slender body reported in [53]. The stagnation zones of the natural and bionic profiles are spread over the short chord region due to small nose tip radiuses. The design with the smallest nose tip radius, the natural design, generates the smallest stagnation zone (Fig. 12a), similarly to the ogive model in [53] at M = 0.8. Just downstream from the nose tip in both cases, Fig. 12a and [53], a similar c_{pi} behaviour is noticed. Here, the c_{pi} distribution shows local disturbance within the zone of a relatively uniform c_{pi} distributed up to $x/$ LC ≈ 0.06, but without a sudden local decrease in values as shown in [53]. The main reason for such pressure variations is found in the difference of the relative radiuses followed by the curviness of these profiles. The c_{pi} distribution over the transition regions has several agreements. The least-bionic profiles, D6 and MIXMOD, have shown the behaviour of the c_{pi} distribution over the foreheads similar to that of the von Karman profile in [53], followed by a similar trend of change of the transition region, and explained by the geometric similarity of the profiles. According to the obtained M_{cr} for the natural and bionic profiles, shown in Fig. 15b, one may note that the sonic lines have appeared at a lower free stream M. In the case of the axis-symmetric projectiles in [53], the sonic lines are not spotted at M = 0.8. Of course, such differences in values are expected because the comparison is done between 2D an axis-symmetric body. However, the zones of flow acceleration are, in both cases, positioned over the transition regions. Again, in both cases, the smoothness of the contour in the transition region prevents the sudden pressure/velocity changes. In the present study, it was found, as also found in [53], that a decrease in the nose tip radius followed by the tangency between the contours of the forehead and the central body, or a smoothed transition zone, leads to the prevention of the sudden pressure changes. Consequently, the profiles with such a geometry definition are capable of flying with higher velocities without creating sonic lines or shock waves. This is important in the conditions when the high-speed train passes the tunnel, noted in [3]. Further on, it was noticed that the naturally curved airfoils (D2, D2F, and D2RAD) have limited or no advantages for implementation in high-speed train design, but they are expected to find their application in small-scale objects, as shown in [53], and in the environment with higher density, such as water.

Besides building awareness of all the limitations, this work is drawing attention to the fact that the used software gives a sufficiently good prediction of the aerodynamic parameters of interest for the design selection process. The development of new codes and methods that will efficiently calculate the basic aerodynamic parameters of flattened airfoils in the range of subsonic and high-subsonic velocities, as presented in this work, is encouraged.

Conclusion

This multidisciplinary research method for bio-inspired design of the airfoils, aiming at the application to the highspeed trains in 2D, consisted of three parts. In order to gain more input data necessary for application in biomimicry, the first part of this work presents different methods and techniques for analysing and describing of the selected kingfisher natural shape. Next, a family of bionic shapes is created based on the natural design by means of adjusting by approximation, by derivation in the form of multi-segment shapes, and, for a single one, by surface velocity adaption. The most time-consuming operation was designs' preparation with calculations. In the third step, the calculations of the pressure coefficient distributions and

drag coefficients, in the range of $M \leq 0.8$, showed a good potential of the bionic airfoils for application to the high-speed train. With awareness of limitations and requirements of the implemented calculation codes, the multidisciplinary research of the natural and bionic airfoils gives sufficiently good results. The quality of the results is confirmed by the results obtained for parabola- and ellipse-like airfoils, under the same conditions, and the data from the literature. The main advantages of the presented method are found in the application of the fast calculating two-dimensional subsonic (the panel method) and transonic (the small transonic differences method) codes which significantly saved time when compared to the CFD, while still obtaining reliable and sufficiently precise results required at the preliminary and conceptual design selection stage. The development of the custom numerical methods and codes, capable of describing a potential flow past the non-typical airfoils, especially those with a blunt trailing edge, in a range up to transonic velocities, is encouraged as a supportive tool in the pre-CFD phase. In addition, a broader systematization of the bionic airfoils with parameterized definitions necessary and planned for the future work, as well as the CFD and the wind tunnel experiments, based on the experiences from the aviation.

Acknowledgements The authors are grateful to the Ministry of Education, Science and Technological Development, the Republic of Serbia, for partial financial support through the Projects TR-35045 and TR 34028 (2011.–2020.). The authors are grateful to Kevin T. Crofton Department of Aerospace and Ocean Engineering, Virginia Tech, USA, Mr. Vladimir Ivanović, General Manager of the HEXAGON Serbia for laser scanning, Ph.D. Mirko Kozić, Research fellow at Military Technical Institute, Belgrade, for kind mentoring and knowledge transfer in fluid dynamics, Ph.D. Boško Rašuo at the University of Belgrade, Faculty of Mechanical Engineering, for knowledge transfer in bionic. We thank Professor Ph.D. Eric Paterson, Head of the Crofton Department of Aerospace and Ocean Engineering, for permitting the use of TSFOIL2, and M.Sc Slaven Linić, Jasmin d.o.o., with Maja Linić, graphic design student, for technical support. Also, we thank all the authors of the open-source software, listed in References, used in this research.

Author contributions Conceptualization and design were contributed by Suzana Linić, Vojkan Lučanin; Methodology was contributed by Vojkan Lučanin, Srdjan Živković, Marko Raković, Slavica Ristić, and Suzana Polić; Formal analysis and investigation were contributed by Suzana Linić, Srdjan Živković, Marko Raković, Slavica Ristić, Bojana Radojković; Writing—original draft preparation, was contributed by Suzana Linić; Writing—review and editing, was contributed by Slavica Ristić, Srdjan Živković, Marko Raković, and Suzana Linić; Supervision was contributed by Vojkan Lučanin. All authors read and approved the final manuscript.

Funding Ministry of Education, Science, and Technological Development of the Republic of Serbia—partial financial supporting through the Projects TR-35045, realized by the University of Belgrade Faculty of Mechanical Engineering, and TR 34028, realized by University of Belgrade, Institute of Chemistry, Technology, and Metallurgy (2011.–2020.).

Availability of data and materials All the data are given in the manuscript.

Code availability Except for TSFOIL2, the used codes are freely available on the internet and referenced. TSFOIL2 is available online for educational purposes. We kindly get the permission for use of TSFOIL2 for implementation in this work from the Kevin T. Crofton Department of Aerospace and Ocean Engineering, Virginia Tech, USA, on which we are thankful.

Compliance with ethical standards

Conflict of interest The authors declare that they have no conflict of interest.

Human and animal rights In this research, no animals have been harmed, experienced the pain or being hurt. The preserved specimen of the kingfisher from the Serbian Natural History Museum's zoological collection was used in the conduct of research.

References

1. Ding S-S, Li Q, Tian A-Q, Du J, Liu J-L (2016) Aerodynamic design on high-speed trains. Acta Mech Sin 32(2):215–232. https ://doi.org/10.1007/s1040 9-015-0546-y
2. Wang R, Zhang J, Bian S, You L (2018) A survey of parametric modelling methods for designing the head of a high-speed train. Proc Inst Mech Eng F J Rail Rapid Transit 232(7):1965–1983. https ://doi.org/10.1177/09544 09718 75655 8
3. Raghunathana R, Kimb H, Setoguchic T (2002) Aerodynamics of high-speed railway train. Prog Aerosp Sci 38:469–514
4. Tian H-Q (2019) Review of research on high-speed railway aerodynamics in China. Transp Saf Environ 1(1):1–21. https ://doi. org/10.1093/tse/tdz01 4
5. Muñoz-Paniagua J, García J, Crespo A (2013) Multi-objective aerodynamic optimization of high-speed trains in tunnels. In: 10th international conference on evolutionary and deterministic methods for design, optimization and control with applications to industrial and societal problems, EUROGEN 2013, 7–9 Oct 2013, Las Palmas de Gran Canaria, España, pp 1–15

6. Sun-Joong K, Ji-Hyun L (2014) The evolutionary changes of the streamlined high-speed locomotives: the quantitative analysis to reveal the changes of bullet motif locomotive design criteria. In: XVIII conference of the iberoamerican society of digital graphics—SIGraDi: design in freedom, blucher design proceedings, vol 1, pp 57–61, www.proce eding s.bluch er.com.br/artic le-detai ls/14224 . Accessed 15 Aug 2020
7. Drela M, Youngren H (2001) XFOIL 6.94 User Guide. http://web. mit.edu/drela /Publi c/web/xfoil /. Accessed 25th Feb 2020
8. Fayemi PE, Wanieck K, Zollfrank C, Maranzana N, Aoussat A (2017) Biomimetics: process, tools and practice. Bioinspir Biomim 12(011002):1–20. https ://doi.org/10.1088/1748-3190/12/1/01100 2
9. Kobayashi K (2005) JFS biomimicry interview series: No.6 "Shinkansen technology learned from an owl?"—The story of Eiji Nakatsu. In JFS Newsletter No.31. Japan for Sustainability. https ://www.japan fs.org/en/news/archi ves/news_id027 795.html. Accessed 18 Mar 2019
10. Cooney CR, Bright JA et al (2017) Mega-evolutionary dynamics of the adaptive radiation of birds. Nature 542(7641):344–347. https ://doi.org/10.1038/natur e2107 4
11. ***, Project Mark My Bird, University of Sheffield, https: //www. markm ybird .org/galle ry/alced o_atthi s/2058. Accessed 18 Aug 2020
12. Das AJ, Murmann DC, Cohrn K, Raskar R (2017) A method for rapid 3D scanning and replication of large paleontological specimens. PLoS ONE 12(7):e0179264. https ://doi.org/10.1371/journ al.pone.01792 64.Acces sed15 Augus t2020
13. Carnaby T (2008) Beat about the Bush: Birds. Jacana Media, Johannesburg
14. Rašuo B (2014) Bionika u dizajnu (Bionics in design, in Serbian). University of Belgrade, Faculty of Mechanical Engineering, Belgrade (electronic book)
15. Sawer P (2011) Mirror image: Kingfisher barely causes a ripple as he dives into the water, (ed. Wildlife Photography/Solent, via Daily Mail) from: goo.gl/B14OKP. Accessed on 22 Feb 2016
16. Gardner R (2006) Alcedo atthis. Animal Diversity Web. https ://anima ldive rsity .org/accou nts/Alced o_atthi s. Accessed 02 Oct 2019
17. Stavenga DG, Tinbergen J, Leertouwer HL, Wilts BD (2011) Kingfisher feathers—colouration by pigments, spongy nanostructures and thin films. J Exp Biol 214:3960–3967
18. Polić-Radovanović S, Ristić S, Jegdić B, Nikolić Z (2010) Metodološki i tehnički aspekti primene novih tehnika u zaštiti kulturne baštine (The methodological and technical aspects of new techniques in protecting the cultural heritage, in Serbian). Institut Goša and Centralni institut za konzervaciju, Belgrade
19. Linić S (2018) Biomimikrija kao metod aerodinamićkog dizajniranja voza velikih brzina (Biomimicry as a method of the high speed train aerodynamical designing, in Serbian). Dissertation, University of Belgrade, Faculty of Mechanical Engineering
20. Hocken RJ, Chakraborty N, Brown C (2005) Optical metrology of surfaces. CIRP Ann 54(2):705–719
21. ***. Hexagon Metrology. ROMER Absolute Arm. Product brochure. http://w3.leica -geosy stems .com/downl oads1 23/hxrom / romer /gener al/broch ures/ROMER %20Abs olute %20Arm %20Pro duct%20Bro chure _en.pdf. Accessed 28 Feb 2018
22. Gerbino S, Del Giudice DM, Staiano G, Lanzotti A, Martorelli M (2016) On the influence of scanning factors on the laser scanner-based 3D inspection process. Int J Adv Manuf Technol 84(9–12):1787–1799
23. Ranzuglia G, Callieri M, Dellepiane M, Cignoni P, Scopigno R (2013) MeshLab as a complete tool for the integration of photos and color with high resolution 3D geometry data, CAA 2012 conference proceedings, pp 406–416
24. ***. Blender. Blender Foundation. http://www.blend er.org. Accessed 28 Feb 2018
25. Cummings RM, Mason WH, Morton SA, McDaniel DR (2015) Applied computational aerodynamics: A modern engineering approach. Part of Cambridge Aerospace Series, USA
26. Anderson JD Jr (2001) Fundamentals of aerodynamics, 3rd edn. McGraw-Hill, New York
27. Vos R, Farokhi S (2015) Introduction to transonic aerodynamics. In: Series: fluid mechanics and its applications 110. Springer, Netherlands
28. Hepperle M (2017) JAVAFOIL User's Guide. https ://www. mh-aerot ools.de/airfo ils/java/JavaF oil%20Use rs%20Gui de.pdf . Accessed 25th Feb 2020
29. Mason WH (2020) Software collection: software for aerodynamics and aircraft design. Kevin T. Crofton Department of aerospace and ocean engineering virginia tech. http://www.dept.aoe. vt.edu/~mason /Mason _f/MRsof t.html. Accessed 25th Feb 2020
30. Murman EM., Bailey FR., Johnson ML (1975) TSFOIL—A computer code for two-dimensional transonic calculations, including wind-tunnel wall effects and wave-drag evaluation. In: Aerodynamic analyses requiring advanced computers, Part II. NASA SP-347:769–788.
31. Yang X-S, Koziel S (eds) (2011) Computational optimization and applications in engineering and industry. In: Studies in computational intelligence 359. Springer
32. Tashnizi ES, Taheri AA, Hekmat MH (2010) Investigation of the adjoint method in aerodynamic optimization using various shape parameterization techniques. J Braz Soc Mech Sci Eng 32(2):176–186
33. Fage A (1927) The flow of air and of an inviscid fluid around an elliptic cylinder and an airfoil of infinite span, especially in the region of the forward stagnation point. Philos Trans 227(647):1–19
34. Rasuo B (2006) An experimental and theoretical study of transonic flow about the NACA 0012 airfoil. In: AIAA 2006-3877, 24th applied aerodynamics conference, San Francisco, California
35. Ristić S, Linić S, Samardžić M (2017) Turbulence investigation in the VTI's experimental aerodynamics laboratory. Therm Sci 21(Suppl. 3):S629–S647. https ://doi.org/10.2298/TSCI1 60130 187R
36. Kuzmin A (2008) Bifurcations of transonic flow past flattened airfoils. hal-00433168
37. Cypionka H, PICOLAY. http://www.picola y.de. Accessed 02 Oct 2016
38. ***. Siemens PLM NX11 documentation, Siemens. https ://docs. plm.autom ation .sieme ns.com/tdoc/nx/11/nx_help/#uid:index . Accessed 28 Feb 2018

39. Huwaldt JA (2001) PlotDigitizer. http://plotd igiti zer.sourc eforg e.net. Accessed 18 Mar 2019
40 . Group of authors. FreeCAD (2016) https: //www.freecadweb. or g. Accessed 18 Mar 2019
41. Andrey Ivashov SMath Studio. https: //en.smath.com/view/SMath Studi o/summa ry. Accessed 18 Mar 2019
42. Standish R, SciDAVis (2017) http://scidav is.sourceforge .net/inde x .html. Accessed 18 March 2019
43. Williams T, Kelley C. Gnuplot, http://www.gnuplo t.info. Accessed 18 Mar 2019
44. ***. InkScape. Free Software Foundation Inc. https ://inksc ape. org. Accessed 18 Mar 2019
45 . Brewster R, PaintNet. dotPDN LLC and Rick Brewster. https :// www.getpa int.net. Accessed 18 Mar 2019
46. ***, GIMP. https ://www.gimp.org/. Accessed 16 Nov 2018
47. Ho D. NotePad++. https ://notep ad-plus-plus.org. Accessed 18 Mar 2019
48 . Faltinsen O (2006) Hydrodynamics of high-speed marine vehicles. Cambridge University Press, Cambridge. https: //doi.org/10.1017/ CBO97 80511 54606 8
49. Martínez A, Vega E, Gaite J, Meseguer J (2008) Pressure measurements on real high-speed trains travelling through tunnels. In: BBAA VI international colloquium on: bluff bodies aerodynamics & applications, Milan, Italy, pp 1–11
50. Schulte-Werning B (2000) A synopsis of aerodynamic and aeroacoustic research for modern high-speed trains. In: European congress on computational methods in applied sciences and engineering, ECCOMAS, Barcelona, pp 1–16
51. Yao S, Guo D, Sun Z, Yang G (2015) A modified multi-objective sorting particle swarm optimization and its application to the design of the nose shape of a high-speed train. Eng Appl Comput Fluid Mech 9(1):513–527. https ://doi.org/10.1080/19942 060.2015.10615 57
52. Li X, Chen G, Zhou D, Chen Z (2019) Impact of different nose lengths on flow-field structure around a high-speed train. Appl Sci 9(21):4573. https ://doi.org/10.3390/app92 14573
53. Sanjay Varma A, Sai Sathyanarayana G, Sandeep J (2016) CFD analysis of various nose profiles. Int J Aerosp Mech Eng 3(3):26–29